Programmably switching the NIR upconversion for orthogonal activation of photoacoustic imaging and on-demand phototherapy

Yang Yang
South China Normal University
Jinshu Huang
South China University of Technology
Wei Wei
South China Normal University
Qin Zeng
South China Normal University
Xipeng Li
South China Normal University
Da Xing
South China Normal University
Bo Zhou
South China University of Technology
Tao Zhang (zt@scnu.edu.cn)
South China Normal University

Article

Keywords: upconversion nanoparticles, photoacoustic imaging, on-demand phototherapy

Posted Date: August 19th, 2021

DOI: https://doi.org/10.21203/rs.3.rs-774960/v1

Version of Record: A version of this preprint was published at Nature Communications on June 7th, 2022.
See the published version at https://doi.org/10.1038/s41467-022-30713-w.

Abstract

Upconversion nanoparticles (UCNPs) based phototheranostics offer significant expectations for the personalized cancer medicine via integrating both modalities of imaging diagnostics and phototherapeutics. However, programmably controlling the photoactivation of imaging and therapy towards the accurate diagnosis with minimum side effects for on-demand therapy has remained challenging due to the lack of ideal switchable UCNPs agents. Herein, we demonstrate a facile strategy to simply switch the near infrared emission at 800 nm from rationally designed UCNPs by modulating the irradiation laser into pulse output. Through synthesis of the theranostic UCNPs-DI agent combining with a photosensitizer and a photoabsorbing agent assembled on the UCNPs, the orthogonal activation of in vivo photoacoustic imaging and photodynamic therapy was further achieved by simply altering the excitation modes from pulse to continuous-wave output upon a single 980-nm laser. Importantly, no obvious harmful effects during photoexcitation caused by reactive oxygen species (ROS) photooxidation and photohyperthermia were generated under imaging modality, which facilitates the long-term and real-time imaging-guidance for the subsequent phototherapy. This work provides a new facile approach for the orthogonal activation of imaging diagnostics and photodynamic therapeutics towards the target cancers.

1 Introduction

Cancer phototheranostics, an emerging combinatorial modality of light-diagnostics and -therapeutics, has been developed as personalized precision medicine to enhance the treatment accuracy and efficiency of conventional phototherapies particularly the representative photodynamic therapy (PDT).[1–7] The clinical-approved PDT methodology refers to the photoactivation of a photosensitizer in the presence of molecular oxygen to generate reactive oxygen species (ROS) for destruction of pathological tissues.[8–10] To date, efforts have been devoted to establish the photodynamic theranostics by developing functional photosensitizers to serve as both an imaging agent and a therapeutic agent.[10–13] However, in light of the limitations of currently available photosensitizers with synchronous activation of both diagnostic and therapeutic signals, the long-term and real-time diagnostic imaging may also induce unnecessary phototoxicity (including photooxidation by ROS and the photo-induced hyperthermia effect) in the normal tissues.[14–16] To meet the demand for precision medicine against cancers, programmable photoactivation of the photosensitizers for the safety imaging and efficient therapy in an orthogonal manner is highly desirable but still challenging due to lack of ideal photoswitchable agents.

Among the reported orthogonal theranostic agents, the lanthanide-doped upconversion nanoparticles (UCNPs) with multiple wavelength-tunable emissions in the visible or near-infrared (NIR) region have been demonstrated to be a remarkable candidate for the development of photoswitchable agents.[17–22] Some orthogonal UCNPs-based platforms were constructed for the programmable activation of the cancer diagnosis and therapy.[23–27] However, in previous studies, the two (or more) excitation laser wavelengths (e.g., 980 and 808 nm) and exquisite agents with core-multi-shells structure designs or different

components are indispensable to achieve the switchable emissions,[28–30] which makes the manufacturing process quite complicated and time-consuming as well as requires complex instruments. Moreover, the orthogonal emissions mainly locate in the UV-visible region such as UV/blue,[31, 32] green/red light.[33–37] The switchable NIR emission is still not achieved, which is believed to be more significant in the phototheranostics.

Interestingly, photon upconversion is a multi-step anti-Stokes process and each step may have a temporal characteristic. This means that some upconversion processes would be sensitive to the excitation duration, consequently generating tunable emission profiles as evident in the full-color emissive nanoparticles upon pulse laser excitation.[38] However, it should be noted that such orthogonal upconversion needs complex core-multi-shell nanoparticles which produce great difficulties in the experimental synthesis. By contrast, we recently constructed a simple migratory core-shell nanostructure toward red/green color switchable output by temporal manipulation of the Er^{3+}-Yb^{3+} interactions under 980 nm single-wavelength excitation.[38, 39] Moreover, the tunable NIR upconversion luminescence can be obtained by constructing suitable transitions in specific lanthanide ions. This result provides new chances for the orthogonal NIR upconversion in a much simpler nanostructure through tuning the pulse widths of a single wavelength excitation, showing a remarkable advantage for bioimaging and phototherapy.

In this study, we report a facile strategy to programmably switch the 800 nm NIR emission in Yb/Tm/Er codoped UCNPs by precisely tuning the pulse width of 980 nm excitation laser to achieve the orthogonal real-time safe photoacoustic imaging and effective photodynamic therapy. We discovered for the first time that the NIR emission of Tm^{3+} at 800 nm in such UCNPs is very sensitive to the excitation laser pulse width. This design markedly reduces the complex core-multi-shell nanostructure and the multiple components as well as the synthetic procedure. We further constructed the upconversion nanocomposite (UCNPs-DI) by surface anchoring the photosensitizer indocyanine green (ICG) dye[40, 41] with response to the switchable upconverting NIR emission and the semiconductor (DPP)[42, 43] with absorption covering the visible emission of the UCNPs. Under the excitation of short-pulse 980 nm laser, the ICG is not activated but the visible emissions of UCNPs can be captured by DPP to generate intense photoacoustic signals with no photodynamic and photothermal effect, which facilitates the long-term and real-time imaging of the in vivo tumors without significant phototoxicity observed. Under the continuous-wave (CW) 980 nm excitation, the switch-on NIR upconversion emission could efficiently activate the PDT effect to afford accurate and effective inhibition of the in vivo tumor growth. Moreover, such UCNPs-DI nanoagent can avoid the harmful effect during photoactivated imaging diagnosis and achieve efficient programmable and orthogonal phototherapy by regulating the laser pulse output upon the single 980-nm irradiation, further highlighting the bioapplications of non-steady-state mediated upconversion nanomaterials.

2 Results

2.1 Mechanistic design of UCNPs with switchable NIR emission

In general, the energy transfer rate in a given sensitizer-activator system depends closely on the energy matching between the emission of sensitizer and the absorption of the activator, which shows a decline following an exponential function of the energy gap (Fig. 1a). The upconversion system with an energy mismatch should result in a relatively slow upconversion process than that of the resonantly coupled system (Fig. 1b), allowing to filtrate such upconversion luminescence by reducing the pulse duration time of the excitation laser. Therefore, the dynamic control of switchable upconversion performance in a much simpler structure nanoparticles becomes highly desirable.

To demonstrate the concept-of-proof, we select Yb^{3+}-Tm^{3+} couple for the NIR upconversion and the Yb^{3+}-Er^{3+} couple toward the red upconversion. Note that there is an energy mismatch between Yb^{3+} ($^2F_{5/2}$) to Tm^{3+} ($^3H_5$) while it is resonant for the Yb^{3+} ($^2F_{5/2}$) and Er^{3+} ($^4I_{11/2}$). The $NaYF_4$:20%Yb,1.5%Er,0.3%Tm nanoparticles were prepared for the switchable red/NIR luminescence under CW and pulse-wave (PW) excitations (Fig. 1c). These UCNPs show uniform nanoparticles with an average diameter of ~26 nm according to the transmission electron microscopy (TEM) images (Figure S1a). The adjacent lattice spacing (~ 0.323 nm) calculated by fast Fourier transform (FFT) analysis corresponds to the (111) crystal plane of hexagonal $NaYF_4$ (Figure S1b), which are in well agreement with the selected-area electron diffraction (SAED) patterns (Figure S1c) and X-ray diffraction (XRD) patterns (Figure S2). Figure 1d shows the upconversion emission spectra under 980 nm excitation. As expected, the red emission of Er^{3+} at 650 nm ($UCL_{650\ nm}$) from its $^4F_{9/2} \rightarrow {}^4I_{15/2}$ transition and NIR emission of Tm^{3+} at 800 nm ($UCL_{800\ nm}$) from its $^3H_4 \rightarrow {}^3H_6$ transition were clearly observed under the CW 980 nm excitation. Intriguingly, upon the pulse 980 nm laser, the UCNPs show a gradually decreased NIR emission with reducing the pulse width to 10 ns, and the emission light intensity ratio of $UCL_{650\ nm}$ to $UCL_{800\ nm}$ dramatically increases from 0.89 to 8.25, as illustrated in Fig. 1d,e and Figure S3. This observation quantifies the UCNPs an ideal NIR photoswitchable candidate to be used to construct the orthogonal theranostic agents.

To further examine the non-steady-state upconversion mechanism, we measured the time-dependent profiles at 650 nm and 800 nm, respectively. As displayed in Fig. 2a, the red upconversion emission exhibits a faster rise time than that of the NIR emission before reaching the steady-state. This observation suggests that the upconversion of the NIR emission of Tm^{3+} indeed needs more time by contrast to the red emission originating from the non-resonant energy transfer from Yb^{3+} ($^2F_{5/2}$) to Tm^{3+} ($^3H_5$). Consequently, the red to NIR emission intensity ratio shows a monotonous decline with the time during the excitation pulse. Hence, reducing the pulse width of the excitation laser become a facial but effective way to switch off the NIR emission. Another merit of this upconversion system lies in the stable color output during a large range of pump power densities (Fig. 2b) and different excitation frequencies (Figure S4), which lays a solid foundation for the subsequent biological application. It should be noted

that a co-doping of Er^{3+} and Tm^{3+} into $NaYF_4$ lattice imposes no impact on their rise time feature (Fig. 2c), which confirms the dynamic manipulation of the NIR switchable output. The total energy transfer processes during the dynamic control of the excitation are schematically illustrated in Fig. 2d. In fact, the presence of Tm^{3+} can promote the red upconversion of Er^{3+} slightly through the energy circling of Er^{3+} ($^4I_{11/2}$) → Tm^{3+} ($^3H_5$) → Er^{3+} ($^4I_{11/2}$) (Figure S5). This is in agreement with the faster rise time of the red upconversion emission of the UCNPs with codoping of Tm^{3+} (Fig. 2e). Taken together, the results clearly confirm the validity of using the non-steady-state excitation towards the remarkable NIR-switchable effect of UCNPs, which has never previously been reported involving the lanthanide-based nanoparticles. In the next, the typical pulse laser with width of 10 ns and 20 Hz was selected for the following phototheranostics investigation.

2.2 Construction and characterization of orthogonal phototheranostic nanoagent

To demonstrate the dynamic control of the orthogonal photodiagnostics and phototherapeutics for the safe imaging-guided on-demand phototherapy, a nanoagent (UCNPs-DI) was synthesized via assembly with a visible-absorbing semiconductor DPP and an NIR-activatable photosensitizer ICG on the surface of the UCNPs (Fig. 3a and Figure S6). The as-prepared DPP possesses high optical absorption extinction coefficient in the visible region of 550–700 nm, ensuring the effective energy transfer from UCNPs to DPP to generate photoacoustic signal via pulsed photoirradiation of the nanoagent. In view of the typical NIR absorption of ICG around 800 nm and the NIR-switchable emission of UCNPs, the photodynamic effect is non-responsive to the short-pulse irradiation of UCNPs-DI, facilitating the safe long-term and real-time photoacoustic imaging. Upon CW 980 nm irradiation, the switching-on NIR emission could activate the ICG to efficiently produce the cytotoxic reactive oxygen species (ROS) for phototherapy. Therefore, the orthogonal control of the designed UCNPs-DI under programmable photoactivation guarantees the safety of imaging and the precision of therapy.

Figure 3b shows dynamic light scattering (DLS) results and transmission electron microscopy (TEM) images of UCNPs and UCNPs-DI nanoagent. On the basis of DLS results, all samples present a narrow size distribution with peaks centered at 26 nm and 106 nm for UCNPs and UCNPs-DI, respectively, confirming a good stabilization of UCNPs and UCNPs-DI. The UCNPs and UCNPs-DI nanoagent seen in TEM could accord with DLS results. Figure 3c presents the absorption spectra of UCNPs, DPP, ICG, and UCNPs-DI. According to the absorption peaks recorded at 650 and 800 nm and the Fourier-transform infrared (FTIR) spectroscopy (Figure S7) of UCNPs-DI, the DPP and ICG were loaded on the nanoagent successfully. The luminescence spectra of UCNPs-DI together with the starting UCNPs were then recorded under the PW/CW excitation of 980 nm laser. As illustrated in Fig. 3d and S8, compared with the starting UCNPs, the visible and NIR emission of UCNPs-DI under CW irradiation was suppressed dramatically due to the energy transfer from UCNPs to DPP and ICG. This was also characterized by the lifetime decline of the 800 nm emission (from 463 to 293 μs, Figure S9).[44,45] These results confirmed the successful construction of the aimed phototheranostic nanoagent UCNPs-DI.

To verify the stability of the nanoagent in aqueous solution and physiological fluids, the absorption of UCNPs-DI in PBS solution and blood serum with different concentrations and times were recorded (Figure S10).[46] The absorption of nanoagent does not show an obvious change under these conditions. Adjusting the pH scope of the PBS solution from 8.5 to 5.0 also did not affect its absorption and UCL emission under both 980 nm PW and CW excitations (Figure S11 and S12).[47] The results show that UCNPs-DI has an excellent consistency in a physiological environment, revealing its high stability under the physiological conditions.

To study the theranostic nanoagent for orthogonal photoacoustic imaging and photodynamic therapy with programmable excitations of CW/PW 980 nm laser, we then evaluated its performance in the photoinduced generation of acoustic effect and singlet oxygen ($^1O_2$) in aqueous solutions. Compared with the starting UCNPs, as depicted in Fig. 3e and S13, we observed a strong and concentration-dependent photoacoustic signal (R^2 = 0.99359) when the UCNPs-DI irradiated with 980 nm pulsed laser (10 ns, 0.5 W/cm^2).[48] The PW irradiation of UCNPs-DI had no obvious photothermal effect, while the temperature of UCNPs-DI solution increased dramatically after exposing to the CW irradiation (0.5 W/cm^2), which suggests that the UCNPs-DI does not induce hyperthermia damage during the photoacoustic diagnosis (Figure S14a). The high photostability was confirmed by the measurement of the 10-min photoirradiation of the sample with 4 cycles (Fig. 3f and S14b).[49] The $^1O_2$ photogeneration of UCNPs-DI was then evaluated using the dye singlet oxygen sensor green (SOSG) as an indicator.[50] Fig. 3g and S15a demonstrated that almost no change was observed for the fluorescence of SOSG at 525 nm in the UCNPs-DI solution with PW 980 nm irradiation, revealing no photodynamic toxicity during the photoacoustic diagnosis. On the contrary, 980-nm CW irradiation of UCNPs-DI can generate abundant $^1O_2$, in which the fluorescence of SOSG increased rapidly within 18 min (Figure S15b).

The above results clearly indicate that the UCNPs-DI produced intense photoacoustic signals with negligible photothermal and photodynamic effect upon 980 nm PW irradiation, providing robust ex-vitro evidence for the feasibility of UCNPs-DI as a safe PA imaging candidate for long-time and real-time diagnose or monitoring the therapeutic treatments. On the other side, switching the 980 nm laser into CW modulation activated the significant photodynamic effect to kill cells in lesions through the generation of adequate reactive oxygen species. The overall results provide substantial supports for us to achieve photoacoustic imaging and photodynamic therapy in an orthogonal manner through programmable excitations of UCNPs-DI by CW/PW 980 nm laser.

2.3 Orthogonally regulated target recognition and photodynamic effect in vitro

The cytotoxicity of the UCNPs-DI with PW (10 ns, 20 Hz, 0.5 W/cm^2) and CW 980 nm (0.5 W/cm^2) irradiation was firstly investigated in detail. The standard MTT assay was performed on human non-small cell human breast adenocarcinoma cancer cells (MCF-7). Figure 4a presents the viability of MCF-7 cancer cells incubated with different concentrations (25, 50, 100, 150, and 200 μg/mL) of PBS (gray),

UCNPs-DI (pink), UCNPs-DI + PW (blue), and UCNPs-DI + CW (red). The cell viability was found still over 90% when the concentration of UCNPs-DI up to 200 μg/mL. Thus, the nanoagent should not influence MCF-7 cells viability when their concentration is less than 200 μg/mL. Significantly, PW irradiation of the cells treated with UCNPs-DI did not induce obvious decrease in the cell viability compared with control cells. By contrast, it shows an evident drop in the cell viability under 980 nm CW excitation. When the MCF-7 cancer cells were incubated with 200 μg/mL UCNPs-DI, the cell viability was found dropping to 28 % in the UCNPs-DI + CW group. At this concentration, as shown in Fig. 4b, light dose-dependent cell-killing effect of UCNPs-DI after incubated for 4 h was recorded when exposure to 980 nm CW irradiation. Remarkably, the cell viability of MCF-7 incubated with UCNPs-DI inhibited dramatically to 27.2% with 0.5 W/cm^2 980 nm continuous lasers for 3 min.

The intracellular ROS generation in the UCNPs-DI + CW group and ROS non-generation in the UCNPs-DI + PW group were also confirmed using confocal laser scanning microscope (CLSM) as shown in Fig. 4c, which is consistent with the ROS detection results in Fig. 3g. In addition, the cell viability results were also verified by calcein AM (live cells staining; green) and propidium iodide (PI, dead cells staining; red) double-staining, respectively (Fig. 4d). The fluorescence imaging results showed that the UCNPs-DI has negligible cytotoxicity under PW irradiation but high photodynamic cytotoxicity under CW irradiation. We then further evaluated the cell damage mechanism of UCNPs-DI + PW/CW using flow cytometry with Annexin V-fluorescein isothiocyanate (FITC)/propidium iodide (PI) staining. The data revealed that in the cells treated with UCNPs-DI and pulsed laser irradiation, 2.67% of cells were stained with Annexin V-FITC and 0.23% cells were stained with PI, suggesting that most cells was undamaged under this condition (Fig. 4e). The measurement taken at the group with UCNPs-DI after 980 nm CW irradiation showed that 33.87% of the cells were stained with FITC and 30.70% of the cells were stained with PI, suggesting that the UCNPs-DI + CW treatment caused obvious membrane damage and massive cell death. In addition, the UCNPs-DI showed negligible inhibitory effects to the normal LO_2 cells with or without the 980 nm PW irradiation (Figure S16). The above results confirmed the evidential potentials of UCNPs-DI as safe photoacoustic imaging candidate. Moreover, the results of UCNPs-DI under the 980 nm CW irradiation have validated the nanoagent as a photoswitchable agent for the effective phototherapy.

2.4 In vivo real-time photoacoustic imaging of tumor

With the intense photoacoustic effect and non-photocytotoxicity of UCNPs-DI validated in vitro and in living cells, we then investigated how to use the agent to overcome certain biological drug delivery barriers for the long-term and real-time photoacoustic imaging of specific tumors (Fig. 5a). The PA imaging is a promising diagnostic imaging technique to monitor the molecular distribution and tumor size/morphology for therapeutical guidance due to its high resolution and noninvasive visualization of tissue structures.[51] After intravenous injection of UCNPs-DI into the MCF-7 tumor-bearing nude mice which were pretreated with either UCNPs or UCNPs-DI, the PA images of tumor region were recorded at times of post-injection in 0, 1, 4, 8, 12 and 24 h, respectively. As depicted in Fig. 5b,d, only very slight PA signal increase was observed over time in the UCNPs cohort. In contrast, the PA signal in the tumor region of the UCNPs-DI pretreated cohort started to be detectable at 4 h post-injection, and the PA signal

intensity gradually increased and reached the maximum at 12 h post-injection (Fig. 5c,d). The PA signal in the UCNPs-DI cohort at 12 h post-injection was determined as 10.8 times greater than that in the UCNPs controls (Fig. 5e). Moreover, the PA signal strength still maintained a relative high level after 24 h post-injection of UCNPs-DI, which further proves UCNPs-DI as an excellent PA diagnosing agent. Taken together, these results indicate that UCNPs-DI provide outstanding real-time PA imaging for definition of the tumor region and precise guidance for the subsequent laser irradiation.

2.5 Orthogonally regulated tumor targeting and therapy in vivo

We further evaluated the photoacoustic imaging-guided “on-demand” PDT efficacy in vivo by using the MCF-7 tumor-bearing mice as the animal model (Fig. 6a).[52] The mice were randomly divided into six groups. The control group was injected with PBS; three groups received laser (PW/CW, 980 nm, 0.5 W/cm^2 for 10 min) or UCNPs-DI i.v. injected alone; the other two groups received UCNPs-DI and then went through PW/CW corresponding irradiation (980 nm, 0.5 W/cm^2 for 10 min). The changes in tumor volume and body weight were then monitored and recorded over the next 21 days. As shown in Fig. 6b, c, after injection of the nanoagent for 12 h and laser exposure to the pulsed laser, no obvious tumor growth inhibition effect was observed on during the whole treatment. By contrast, the tumor received the nanoagent and CW 980 nm laser treatment, the volume shrunk persistently, and the tumor growth was almost completely inhibited after treatment for 21 days, as also depicted in Fig. 6d. Figure 6e shows few changes in the body weight of the mice during feeding time, indicating that UCNPs-DI possesses high therapeutic efficiency and the systemic toxicity of the UCNPs-DI nanoagent with PW/CW irradiation was insignificant.

In order to further confirm the anti-tumor effect of UCNPs-DI, we used immunohistochemical staining for histological analysis to evaluate the pathological changes of the tumor tissue collected after the above treatment (Fig. 6f). Tumor sections revealed almost no cell necrosis and apoptosis in the nanoagent cohort with PW irradiation treatment, while the highest level of tumor cell damage was observed in the nanoagent cohort with CW irradiation treatment. In addition, we also performed hematoxylin and eosin (H&E) staining assays to study tumor cell death and organ damage after the phototherapy on the 21st day (Fig. 6g). The images of H&E staining demonstrated the tumor in the CW laser PDT group revealed significantly inhibited proliferation capability of the tumor cells, which is in agreement with the therapeutic results of the above-mentioned immunohistochemical staining in vivo. The photographs of the pathomorphological analysis of heart, liver, spleen, lung, and kidney are provided in Figure S17, which shows no obvious organ damage in all cases, indicating that the prepared UCNPs-DI nanocomposite have very good biocompatibility in vivo. Taken together, these results reveal that we can achieve the in vivo orthogonal safe PA imaging and highly effective phototherapy in the UCNPs-approved nanoagent through programmablly switching the on-duty ratio of the excitation laser with the same wavelength.

3 Discussion

In summary, we have successfully demonstrated a facile but efficient strategy to switch the NIR 800 nm emission of the UCNPs by programmablly regulating the on-duty ratio of the excitation laser to achieve the orthogonal real-time safe photoacoustic imaging and effective “switching on-demand” photodynamic therapy with a rational design nanoagent. The nanoagent UCNPs-DI is composed of a highly visible-absorbing semiconductor DPP and an NIR photosensitizer ICG loaded on the surface of the typical Er^{3+}/Tm^{3+}-doped UCNPs. The nanoagent with programmablly controlling upconversion process can efficiently transduce the 980 nm excitation to the steady-state visible light and dynamic NIR light. The spectral overlap between the absorption of DPP and the upconverted visible emission makes better use of the highly emissive upconversion for photoacoustic imaging for determining the lesion area under 980 nm pulsed laser, under which conditions, no photothermal and photodynamic effect can be activated. By switching the excitation light into CW mode to lighten the 800 nm emission, the ICG can be activated to generates cytotoxic ROS for antitumor therapy. In short, with UCNPs-DI, we can avoid the harmful effects caused by the ROS photooxidation and photohyperthermia during the long-term and real-time PA imaging diagnosis and achieve effective PA imaging-guided phototherapeutics. This work provides a new facile approach for the orthogonal activation of imaging diagnostics and photodynamic therapeutics towards the target cancers.

4 Experimental Methods

4.1 Materials

The chemicals mentioned in this article were all reagent grade and can be used immediately without further purification and filtration. Rare earth chlorides $X(CH_3COO)_3{\cdot}4H_2O$ (X = Yb, Y), $Y(CH_3COO)_3{\cdot}xH_2O$ (Y = Er, Tm). 1-octadecane (ODE), NaOH, Oleic acid (OA), Ammonium fluoride (NH_4F), ICG (Indocyanine Green). were purchased from Sigma-Aldrich Corporation (MO, USA); 5,50-dibromo-2,20-dithiophene (TH) and 3,6-Bis(5-trimethylstannylthien-2-thienyl)-2,5-bis(2-decyltetradecyl)-2,5-dihydropyrrolo[3,4-c]pyrrole-1,4-dione (DPP) were used and purchase as received from Derthon Optoelectronic Materials Science & Technology Co., Ltd. (Shenzhen, China). DSPE-PEG-COOH(1,2-distearoyl-sn-glycero-3-phosphoethanolamine-N-[methoxy(polyethyleneglycol)-2000) was purchased from Avanti Polar Lipids Inc. (AL, USA). SOSG was obtained from Thermo Fisher Scientific Co, Ltd. (China), FBS (Fetal bovine serum), DMEM (Dulbecco’s modified Eagle’s medium) and penicillin were used and purchase as received from GIBCO. 3-(4,5-Dimethylthiazol-2-yl)-2,5-diphenyltetrazolium bromide (MTT), calcein-AM (calcein-acetylmethoxylate), PI (propidium iodide) and FITC (4-nitrophthalonitrile fluorescein isothiocyanate) were used from Sigma-Aldrich Corporation (MO, USA). Ultrapure water comes from Millipore Milli-Q water purification system (Billerica, USA).

4.2 Characterizations

The absorbance values of UCNPs and UCNPs-DI were measured by an ultraviolet/visible absorption spectrometer (Lambda-35 UV/visible spectrophotometer, Perkin-Elmer, MA, USA). Upconversion fluorescence emission of UCNPs and UCNPs-DI were obtained using 500 mW/cm2 980 nm laser was

surveying. Obtain the fluorescence spectra of UCNPs and UCNPs-DI on the spetrasuite software.The TEM image of UCNPs and UCNPs-DI is a high-resolution 2100F field emission transmission electron microscope (JEOL, Japan) operating at a capture acceleration voltage of 200 kV. ZEN3690 zeta sizer (Malvern, USA) was used to measure the size of nanoagent. At room temperature, in the Bio-Rad FTS 6000 spectrometer (Bio-Rad Company, Hercules, California, USA) recorded in FT-IR spectrum in the form of KBr particles. UCNPs and UCNPs-DI stability by getting in different pH (from pH 5.0 to 8.5) the absorption and fluorescence spectra assessed UCNPs-DI.

4.3 Synthesis of UCNPs-DI

1 μmol DSPE-PEG-$COOH_2$ was dispersed in 1 ml deionized water, next 400 μL of tetrahydrofuran solution, which contains DPP (0.4 mg/mL), UCNPs (2 mg/mL), ICG (0.1 M) were dissolve to the DSPE-PEG-$COOH_2$ solution. The solution was sonicated for 10 minutes and stirred overnight at 37°C. After centrifuging the solution to obtain the crude product, the crude product was scrubbed 3 times with deionized water for further functionalization. The final nanoagent (UCNP-DI) obtained was redispersed in PBS solution and deposited in 4°C.

4.4 Detection of singlet oxygen production.

Using Singlet Oxygen Sensor Green (SOSG) to detect UCNPs-DI under 980 nm pulsed laser and continuous laser conditions. First of all, Singlet Oxygen Sensor Green (SOSG) is a highly selective detection reagent for singlet oxygen. Then dissolve SOSG (33 μL) in ethanol and neutralize the solution with 3 mL of PBS. Finally, the SOSG solution (100 μL) was appended to 1 mL of UCNPs-DI solution of different concentrations. The solution was irradiated under 980 nm continuous laser and pulsed laser radiation (0.5 W/cm^2). Perkin-Elmer was used to record the emission intensity of various solutions (measure fluorescence intensity using 488 nm excitation and 525 nm emission).

4.5 Cell culture and Cytotoxicity testing

MCF-7 (Human breast adenocarcinoma cells) were cultured in 1% and penicillin/streptomycin DMEM containing 10% fetal bovine serum after gamma irradiation and sterile filtration. The culture environment of MCF-7 cells is a humid environment with a temperature of 37°C and a CO_2 concentration of 5%.

Using MTT reagent to evaluate the cytotoxicity of UCNPs-DI. The MCF-7 cells were first planted in a 96-well plate and cultured in 5% CO_2 at 37°C for 24 hours. Then remove the medium from the 96-well plate of full MCF-7 cells and rinse with PBS. Afterwards, MCF-7 was pretreated with UCNPs-DI (concentrations of 0, 25, 50, 100, 150, and 200 μg/mL) solution for 4 hours. Then the 96-well plate was irradiated under 980 nm pulsed laser and continuous laser (0.5W/cm^2,3 minutes). Next the cells were incubated for 24 hours, added 10 μL MTT to the 96-well plate for an additional 4 hours incubation, and added 100 μL SDS was added at 4 hours for another 4 hours of incubation. We will use a microplate reader to measured and recorded the absorbance of MTT (Infinite 200, TECAN, Switzerland). Finally, cell viability is determined by the following equation: cell viability (%) = (average absolute value of the treatment group/average absolute value of the control) ×100%.

4.6 Intracellular $^1O_2$ detection

Inoculated and cultured MCF-7 tumor cells in a 35 mm confocal culture dish and continue to grow for 24 hours. After that, the MCF-7 cells cultured in DMEM medium were incubated with UCNPs-DI (200 μg/mL) for 4 hours. After removing the medium in the confocal dish and washing the cells with PBS. Confocal fluorescence imaging of UCNPs-DI was recorded at 500–550 nm by confocal laser scanning microscope (ZEISS LSM 510 META, Germany) under 980 nm laser.

First, the MCF-7 cells in the confocal culture dish were treated with UCNPs-DI (200 μg/mL) nanoagents and 5 μM SOSG methanol solution (50 μL) and incubated for 4 hours in a humidified incubator at 37°C in the dark. Next, use a 980 nm pulsed laser with a power of 0.5 W/cm^2 for 3 minutes. Observe and record the SOSG fluorescence emission through the confocal microscope imaging system (the excitation light of SOSG is 488 nm, and the fluorescence emission is 525 nm). Under the same conditions, the other group was irradiated with a 980 nm continuous laser (0.5W/cm^2, 3 minutes), observed and recorded.

4.7 Tumor mouse model

All animal experiments comply with the Guidelines for the Care and Use of Laboratory Animals issued by the National Institutes of Health (NIH) of South China Normal University, and all animal experiments have been approved and approved by the Animal Ethics Committee of South China Normal University. Female BALB/C nude mice (4 weeks) were acquired from the Animal Experiment Center of Southern Medical University and raised in a sterile mouse house.

Female BALB/ C nude mice aged 4 weeks were purchased from the Animal Experimental Center of Southern Medical University and raised in a sterile environment. The MCF-7 tumor cells were transferred and evenly distributed in 100 μL PBS, and injected subcutaneously into the right abdomen of each mouse.When the tumor reached about 100 mm^3, the animals were tested. The calculation formula of tumor volume is: tumor volume = length (maximum longitudinal diameter) × width (maximum transverse diameter)^2 × 0.5.

4.8 Photoacoustic imaging in tumor in vivo

In addition, Balb/c mice carrying MCF-7 cells were divided into 6 groups. The blank group was injected with PBS only; the 980 nm group was focused with980 nm pulsed light and continuous light laser (0.5 W/cm^2, 10 minutes); the mice in the UCNPs-DI group were injected intravenously with 100 μL UCNPs-DI (200 μg/mL). The treatment group used 100 μL UCNPs-DI (200 μg/mL) and 980 nm continuous and pulsed laser (0.5 W/cm^2, 10 minutes) to focus on the tumor area for 10 minutes, respectively. Finally, the 6 groups of mice were injected with UCNPs-DI through the tail vein every 2 days, and the tumor area was treated with laser 12 hours later. During the treatment, the mice were anesthetized with oxygen containing 2.5% isoflurane. The treatment effects of the 6 cohorts were appraised by detecting and recording the relative tumor volume and weight changes of mice.

4.9 Detection of singlet oxygen in vivo.

Mice with MCF-7 tumors were intravenously injected with 200 μg/mL UCNPS-DI (100 μL). At the time point 12 hours after the injection, 50 μM SOSG (30 μL) was injected into the tumor tissue of the mouse. Then, 980 nm continuous light and pulsed light were used to irradiate the tumor area at a power density of 0.5 W/cm^2 (10 minutes). After the mice were euthanized, the tumor tissues of the mice were dissected, and the tumor tissues were fixed in 4% paraformaldehyde. Frozen sections are 10 μm thick. Finally, the tumor slices were blurred with SOSG, then recorded and observed under the Olympus FV3000 confocal laser scanning microscope.

4.10 Histology examination

After the treatment, the mice were euthanized. The tumor tissues and major organs (heart, liver, spleen, lung and kidney) were removed from 6 groups of mice and cut into sections with thickness of 4 μm. The tumor sections were fixed in 10% paraformaldehyde solution for 12 h, then dehydrated with ethanol and processed into paraffin. Finally, the tissue section was stained with H&E and recorded and imaged by a fluorescence microscope system (Nikon E 200). The H&E staining method is processed according to the method provided by the supplier (BBC Biochemical)

Declarations

Conflicts of interest

The authors declare no competing financial interests.

Data availability statement

The raw/processed data required to reproduce these findings are available from the authors.

Acknowledgments

This research was supported by the National Natural Science Foundation of China (21771065, 51972119), the Guangdong Special Support Program (2017TQ04R138), the Natural Science Foundation of Guangdong Province, China (2019A1515012021), and the State Key Laboratory of Luminescent Materials and Devices, South China University of Technology (Skllmd-2021-01).

References

1. J. Ge, et al. A graphene quantum dot photodynamic therapy agent with high singlet oxygen generation. *Nat. Commun.* **5**, 4596 (2014).
2. D. Wang, et al. Self-assembled single-atom nanozyme for enhanced photodynamic therapy treatment of tumor. *Nat. Commun.* **11**, 357 (2020).
3. Z. Huang A review of progress in clinical photodynamic therapy. *Technol. Cancer. Res. T.* **4**, 283–293 (2005).

4. D. E. J. G. J. Dolmans, D. Fukumura &R. K. Jain Photodynamic therapy for cancer. *Nat. Rev. Cancer* **3**, 380–387 (2003).
5. Z. Yu, P. Zhou, W. Pan, N. Li &B. Tang A biomimetic nanoreactor for synergistic chemiexcited photodynamic therapy and starvation therapy against tumor metastasis. *Nat. Commun.* **9**, 5044 (2018).
6. J. Xu, et al. Highly emissive dye-sensitized upconversion nanostructure for dual-hotosensitizer photodynamic therapy and bioimaging. *Acs Nano* **11**, 4133–4144 (2017).
7. L.-H. Liu, et al. A red light activatable multifunctional prodrug for image-guided photodynamic therapy and cascaded chemotherapy. *Adv. Funct. Mater.* **26**, 6257–6269 (2016).
8. Q. Zeng, R. Zhang, T. Zhang &D. Xing H_2O_2-responsive biodegradable nanomedicine for cancer-selective dual-modal imaging guided precise photodynamic therapy. *Biomaterials 207*<bi>,</bi> 39–48 (2019).
9. C. Liu, et al. An open source and reduce expenditure ROS generation strategy for chemodynamic/photodynamic synergistic therapy. *Nat. Commun.* **11**, 1735 (2020).
10. H. Kim, Y. Kim, I.-H. Kim, K. Kim &Y. Choi ROS-responsive activatable photosensitizing agent for imaging and photodynamic therapy of activated macrophages. *Theranostics* **4**, 1–11 (2013).
11. F. Hu, et al. Metal–organic framework as a simple and general inert nanocarrier for photosensitizers to implement activatable photodynamic therapy. *Adv. Funct. Mater.* **28**, 1707519 (2018).
12. Y. Shen, et al. ATP-activatable photosensitizer enables dual fluorescence imaging and targeted photodynamic therapy of tumor. *Anal Chem.* **89**, 13610–13617 (2017).
13. C. Wang, H. Tao, L. Cheng &Z. Liu Near-infrared light induced in vivo photodynamic therapy of cancer based on upconversion nanoparticles. *Biomaterials 32*, 6145–6154 (2011).
14. R. Lv, et al. A yolk-like uultifunctional platform for multimodal imaging and synergistic therapy triggered by a single near-Infrared light. *ACS Nano* **9**, 1630–1647 (2015).
15. Yansong, et al. Assembly of upconversion nanophotosensitizer in vivo to achieve scatheless real-time imaging and selective photodynamic therapy. *Biomaterials* **201**, 33–41 (2019).
16. H. Li, et al. Temporal multiplexed in vivo upconversion imaging. *J. Am. Chem. Soc.* **142**, 2023–2030 (2020).
17. R. Deng, et al. Temporal full-colour tuning through non-steady-state upconversion. *Nat. Nanotechnol.***10**, 237–242 (2015).
18. H. Suo, C. Guo &T. Li Broad-scope thermometry based on dual-color modulation up-conversion phosphor $Ba_5Gd_8Zn_4O_{21}$:Er^{3+}/Yb^{3+}. *J. Phys. Chem. C* **120**, 2914–2924 (2016).
19. Q. Chen, et al. Confining excitation energy in Er^{3+}-sensitized upconversion Nanocrystals through Tm^{3+}-mediated transient energy trapping. *Angew. Chem. Int. Ed.* **56**, 7605–7609 (2017).
20. B. Zhou, et al. NIR II-responsive photon upconversion through energy migration in an ytterbium sublattice. *Nat. Photonics* **14**, 760–766 (2020).

21. X. Li, et al. Filtration shell mediated power density independent orthogonal excitations–emissions upconversion luminescence. *Angew. Chem. Int. Ed.* **55**, 2464–2469 (2016).
22. F. Wang, et al. Tuning upconversion through energy migration in core–shell nanoparticles. *Nat Mater.* **10**, 968–973 (2011).
23. P. Wang, et al. Orthogonal near-infrared upconversion co-regulated site-specific O_2 delivery and photodynamic therapy for hypoxia tumor by using red blood cell microcarriers. *Biomaterials* **125**, 90–100 (2017).
24. Z. Zhang, et al. Upconversion superballs for programmable photoactivation of therapeutics. *Nat. Commun.***10**, 4586 (2019).
25. Z. Zhang, et al. Modularly assembled upconversion nanoparticles for orthogonally controlled cell imaging and drug delivery. *ACS Appl. Mater. Interfaces* **12**, 12549–12556 (2020).
26. Z. Zhang &Y. Zhang Orthogonal emissive upconversion nanoparticles: material design and applications. *Small* **17**, 2004552 (2021).
27. F. Zhang, et al. Precise in vivo inflammation imaging using in situ responsive cross-linking of glutathione-modified ultra-small NIR-II lanthanide nanoparticles. *Angew. Chem. Int. Ed.* **131**, 2072–2076 (2019).
28. Z. Di, et al. An orthogonally regulatable DNA nanodevice for spatiotemporally controlled biorecognition and tumor treatment. *Sci. Adv.* **6**, eaba9381 (2020).
29. M. Tang, et al. Near-infrared excited orthogonal emissive upconversion nanoparticles for imaging-guided on-demand therapy. *ACS Nano* **13**, 10405–10418 (2019).
30. J. Zuo, et al. Near infrared light sensitive ultraviolet–blue nanophotoswitch for imaging-guided “off–on” therapy. *ACS Nano* **12**, 3217–3225 (2018).
31. X. Chen, et al. Confining energy migration in upconversion nanoparticles towards deep ultraviolet lasing. *Nat. Commun.* **7**, 10304 (2016).
32. J. Li, H. Duan &K. Pu Nanotransducers for near-infrared photoregulation in biomedicine. *Adv. Mater* **31**, 1901607 (2019).
33. M. Wu, L. Yan, T. Wang, B. Zhou &Q. Zhang Controlling red color–based multicolor upconversion through selective photon blocking. *Adv. Funct. Mater* **29**, 1804160 (2019).
34. H. Wang, Z. Wang, Y. Gu A novel theranostic nanoprobe for in vivo singlet oxygen detection and real-time dose–effect relationship monitoring in photodynamic therapy. *Small* **15**, 1–11(2019).
35. B. Zhou, et al. Constructing interfacial energy transfer for photon up- and down-conversion from lanthanides in a core-shell nanostructure. *Angew. Chem. Int.Ed.* **128**, 12544–12548 (2016).
36. C. Wang, L. Cheng &Z. Liu Upconversion nanoparticles for photodynamic therapy and other cancer therapeutics. *Theranostics* **3**, 317–330 (2013).
37. A. Punjabi, et al. Amplifying the red-emission of upconverting nanoparticles for biocompatible clinically used prodrug-induced photodynamic therapy. *ACS Nano* **8**, 10621–10630 (2014).

38. J. Huang, et al. Dynamic control of orthogonal upconversion in migratory core–shell nanostructure toward information security. *Adv. Funct. Mater.* **31**, 2009796 (2021).
39. L. Li, F. Pan, P. A. Tanner &K.-L. Wong Tunable dual visible and near-infrared persistent luminescence in doped zinc gallogermanate nanoparticles for simultaneous photosensitization and bioimaging. *ACS Appl. Mater. Interfaces* **3**, 1961–1971 (2020).
40. C. Fang, et al. Multifunctional MoO_2-ICG nanoplatform for 808nm-mediated synergetic photodynamic/photothermal therapy. *Appl. Mater. Today* **15**, 472–481 (2019).
41. J. F. Callan, J. Atchison, S. Kamila, H. Nesbitt &A. P. Mchale Iodinated cyanine dyes: a new class of sensitisers for use in NIR activated photodynamic therapy (PDT). *Chem. Commun.* **53**, 2009–2012 (2017).
42. H. Chen, et al. Highly absorbing multispectral near-infrared polymer nanoparticles from one conjugated backbone for photoacoustic imaging and photothermal therapy. *Biomaterials* **144**, 42–52 (2017).
43. Y. Yang, T. Zhang &D. Xing Single 808 nm NIR-triggered multifunctional upconverting phototheranostic nanocomposite for imaging-guided high-efficiency treatment of tumors. *J. Biophotonics*, **134**, 1–14 (2021).
44. X. Ai, et al. In vivo covalent cross-linking of photon-converted rare-earth nanostructures for tumour localization and theranostics. *Nat. Commun.***7**, 10432 (2016).
45. Y. Lu, et al. Tunable lifetime multiplexing using luminescent nanocrystals. *Nat. Photonics* **8**, 32–36 (2014).
46. J. Zheng, Y. Wu, D. Xing &T. Zhang Synchronous detection of glutathione/hydrogen peroxide for monitoring redox status in vivo with a ratiometric upconverting nanoprobe. *Nano Res.* **12**, 931–938 (2019).
47. X. Jin, Q. Zeng, J. Zheng, D. Xing &T. Zhang Aptamer-functionalized upconverting nanoformulations for light-switching cancer-specific recognition and in situ photodynamic–chemo sequential theranostics. *ACS Appl. Mater. Interfaces* **13**, 9316–9328 (2020).
48. K. Pu, et al. Semiconducting polymer nanoparticles as photoacoustic molecular imaging probes in living mice. *Nat. Nanotechno.* **9**, 233–239 (2014).
49. X. Zhu, et al. Temperature-feedback upconversion nanocomposite for accurate photothermal therapy at facile temperature. *Nat. Commun.* **7**, 10437 (2016).
50. C. Wang, et al. Specific generation of singlet oxygen through the russell mechanism in hypoxic tumors and GSH depletion by Cu-TCPP nanosheets for cancer therapy. *Angew. Chem. Int. Ed.* **58**, 9846–9850 (2019).
51. J. Zheng, Q. Zeng, R. Zhang, D. Xing &T. Zhang Dynamic-reversible photoacoustic probe for continuous ratiometric sensing and imaging of redox status in vivo. *J. Am. Chem. Soc.* **141**, 19226–19230 (2019).

52. Y. Jiang, J. Huang, C. Xu &K. Pu Activatable polymer nanoagonist for second near-infrared photothermal immunotherapy of cancer. *Nat. Commun.***12**, 742 (2021).

Figures

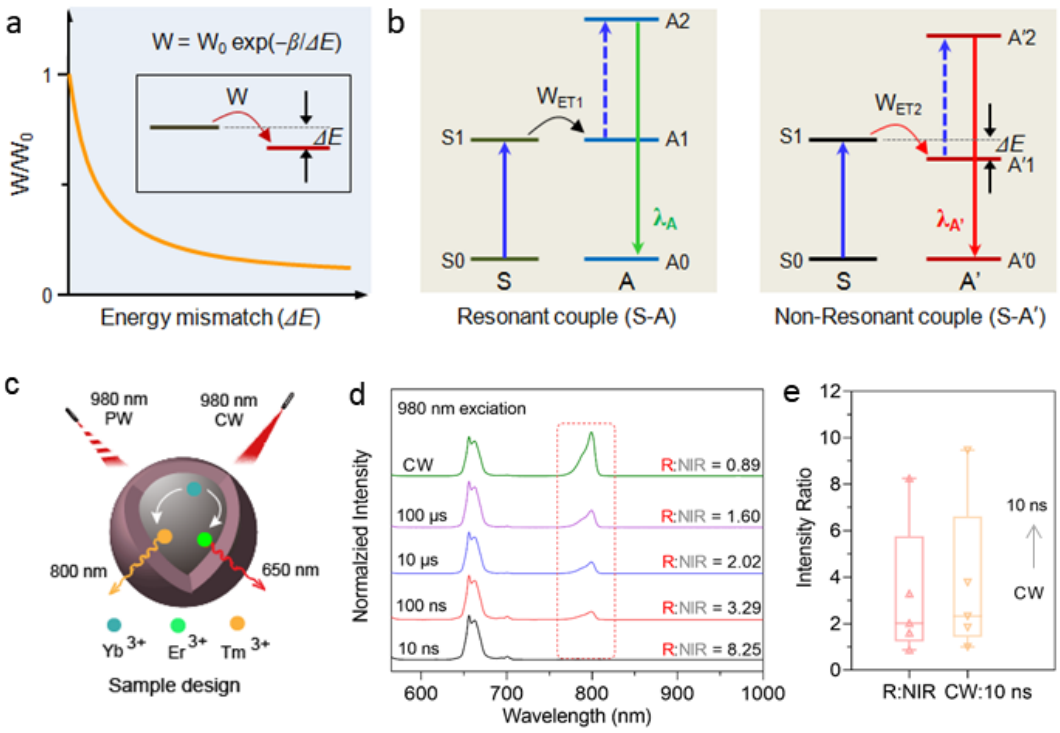

Figure 1

Mechanistic design towards NIR switchable upconversion. (a) Schematic of energy transfer rate (W) depending on the energy mismatch (ΔE) between the relevant energy levels of sensitizer (S) and activator (A). Inset shows the non-resonant energy transfer process from S to A. Note that W0 is the rate when ΔE = 0, and β presents a positive parameter. (b) Comparison of the resonant (left) and non-resonant (right) sensitizer-activator coupled upconversion systems. (c) Schematic of the orthogonal emissive properties of the specially designed UCNPs, i.e., red emission with 980 nm continuous laser light and red/NIR emission with 980 nm pulsed laser light excitation. (d) Upconversion emission spectra of the UCNPs obtained by the used of different pulsed durations, demonstrating the ratio of 650 nm and 800 nm

emission intensities. (e) Red-to-NIR and NIR luminescence intensity ratios as an orthogonal emissive upconversion nanoparticles under 980 nm excitation.

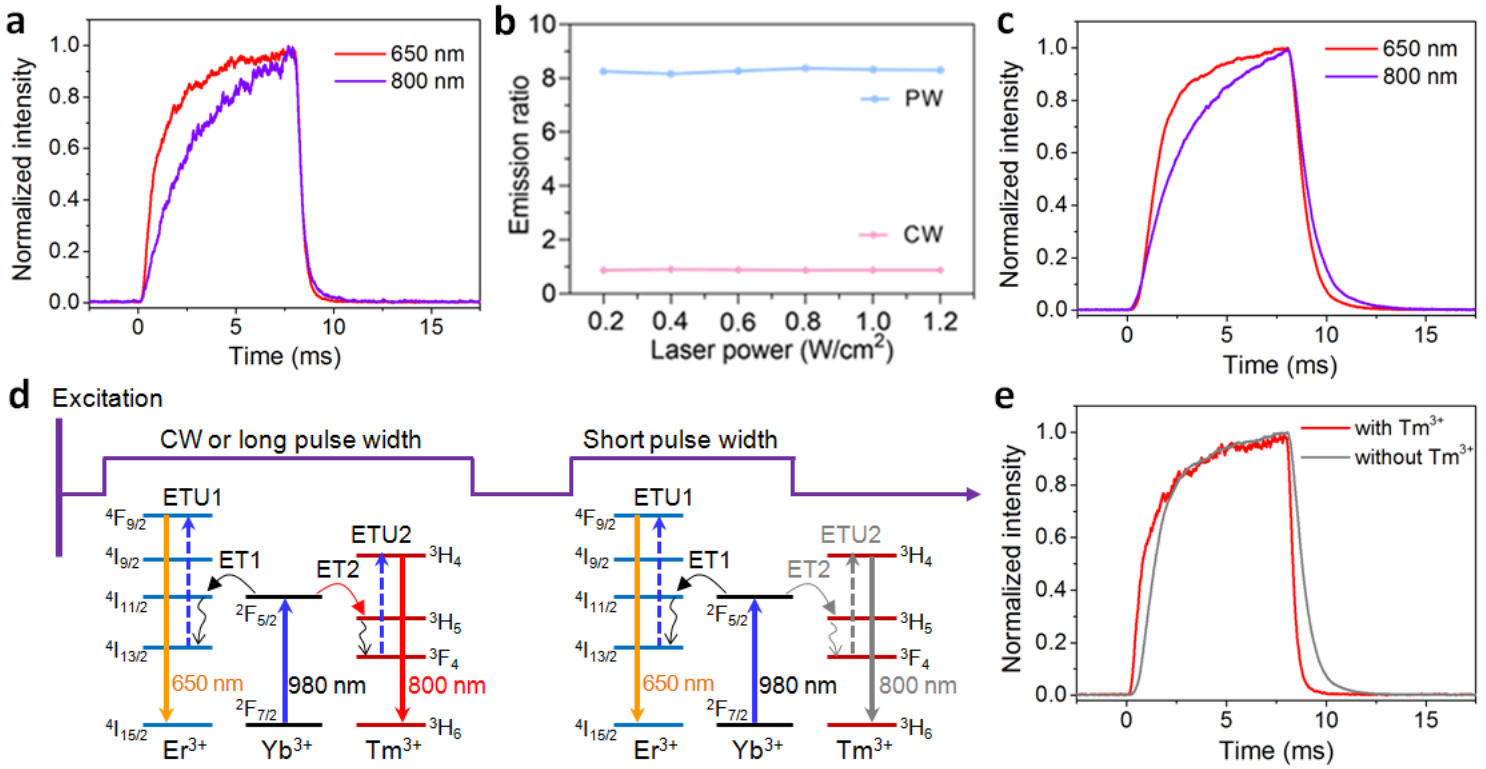

Figure 2

Switchable NIR upconversion mechanism through non-steady-state excitation. (a) Time-dependent upconversion emission profiles of Er3+ at 650 nm and Tm3+ at 800 nm for the UCNPs under 980 nm excitation with a duration time of 8 ms. (b) Dependence of the red/NIR ratio of the UCNPs on pump power density upon 980 nm excitation with CW and PW (with width of 10 ns) laser. (c) Time-dependent upconversion emission profiles of Er3+ at 650 nm and Tm3+ at 800 nm for the UCNPs doping with only Er3+ and Tm3+, respectively, under 980 nm excitation with a duration time of 8 ms. (d) Schematic dynamic control of upconversin in Yb3+/Er3+/Tm3+ codoped system for 650 nm red and switchable 800 nm NIR emissions under 980 nm excitation with CW or PW laser. (e) Comparison of the time-dependent upconversion emission profiles of Er3+ at 650 nm for the UCNPs with and without codoping of Tm3+ under 980 nm excitation with a duration time of 8 ms.

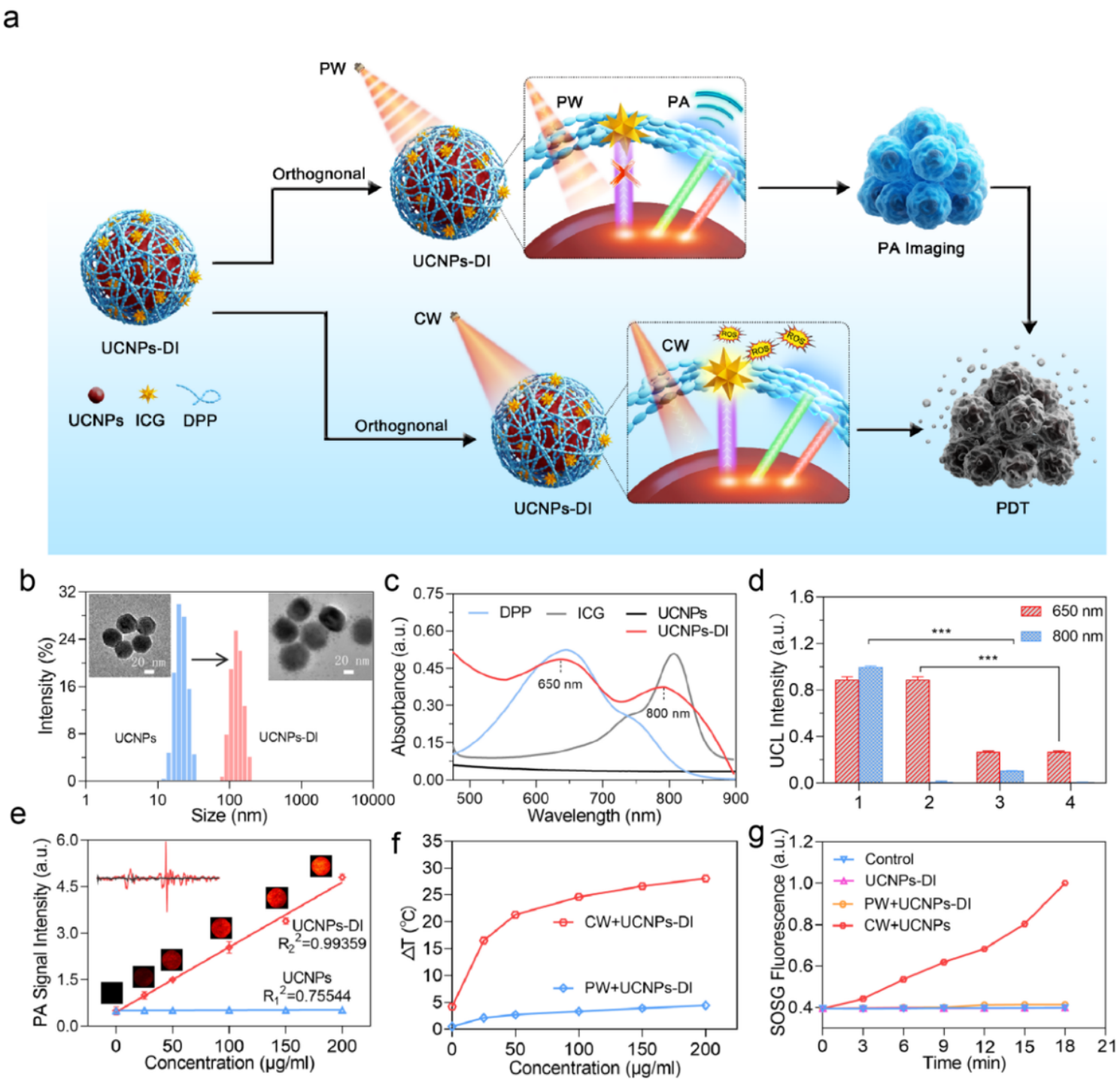

Figure 3

Design and characterization of the orthogonal UCNPs-DI nanoagent. (a) Schematic showing the orthogonal regulation of UCNPs-DI for photoacoustic imaging-guided “on-demand” treatment. (b) TEM imaging and Dynamic Light Scattering (DLS) of UCNPs, UCNPs-DI respectively. Scale bars are 20 nm. (c) UV–vis absorption a spectrum of UCNPs, ICG, DPP, and UCNPs-DI, respectively. (d) Upconversion emission spectra of CW+UCNPs (1) PW+UCNPs (2) CW+UCNPs-DI (3) PW+UCNPs-DI (4) at 650 nm and 800 nm. (*p < 0.05, **P < 0.001, ***P < 0.0001). (e) PA intensity of UCNPs-DI as a function of concentration (R2 = 0.99359), and the inset shows the single PA signal. (f) Temperature changes of UCNPs-DI under

irradiation of 980 nm PW or CW at the same power density (0.5 W/cm2). (g) Normalized SOSG fluorescence in the presence of UCNPs-DI upon different treatment group.

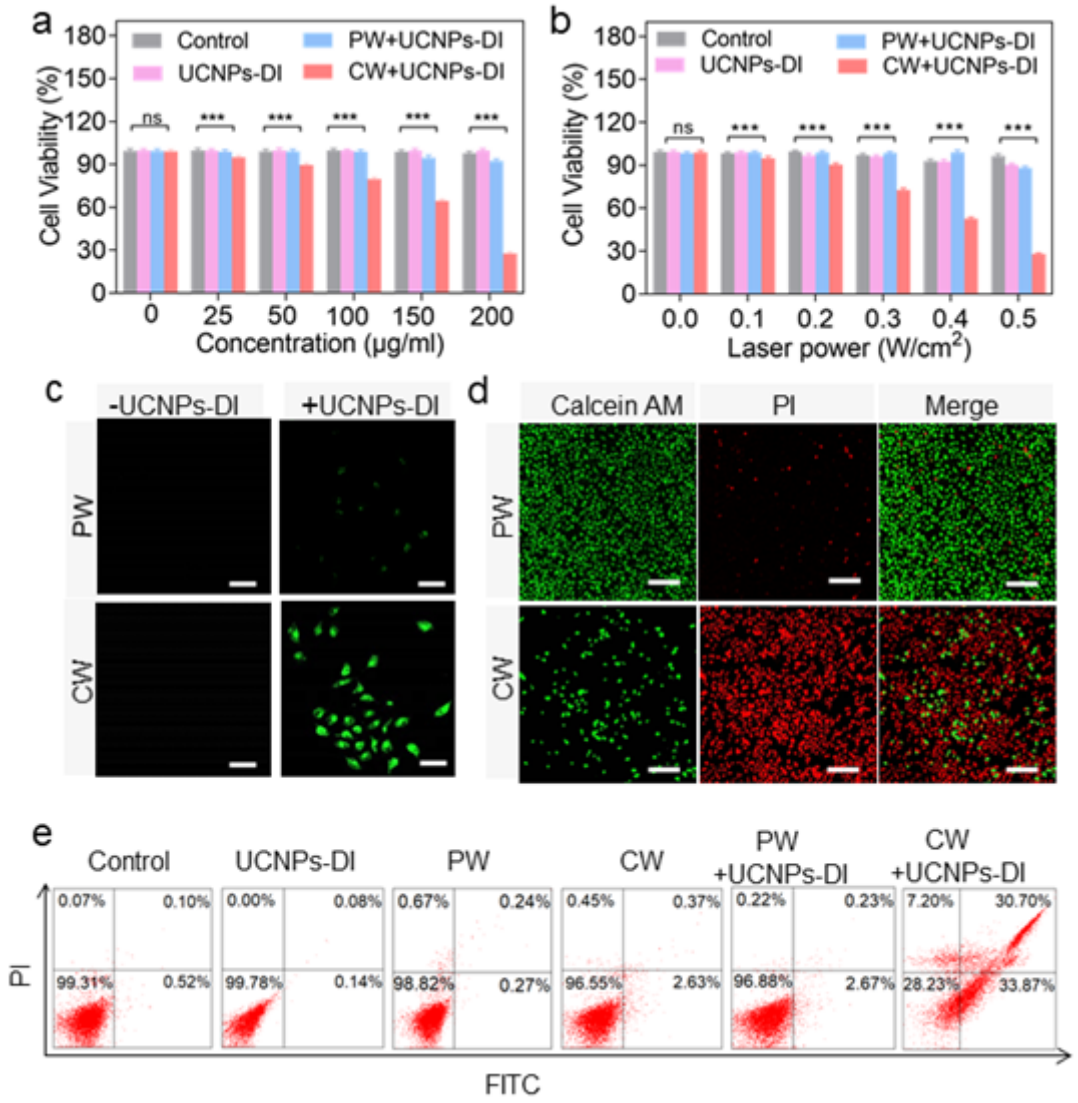

Figure 4

Cytotoxicity of UCNPs-DI in the orthogonal excitation. (a) Relative viabilities of MCF-7 cells incubated with UCNPs-DI in different concentration under 980 nm pulsed laser and 980 nm continuous laser. (b) Relative viabilities of cells treated with different laser power. (c) Microscopic images of the MCF-7 cells incubated with 200 μg/mL UCNPs-DI for 4 h with different treatments (untreated + SOSG, SOSG) after 980 nm irradiation (0.5 W/cm2, 3 min). (d) Confocal fluorescence microscope images of calcein AM and PI co-stained MCF-7 cells after various treatments indicated. Green and red colors represented live and dead cells, respectively in 980 nm pulsed laser and 980 nm continuous laser. (e) Flow cytometric analysis of MCF-7 cells death after different treatments.

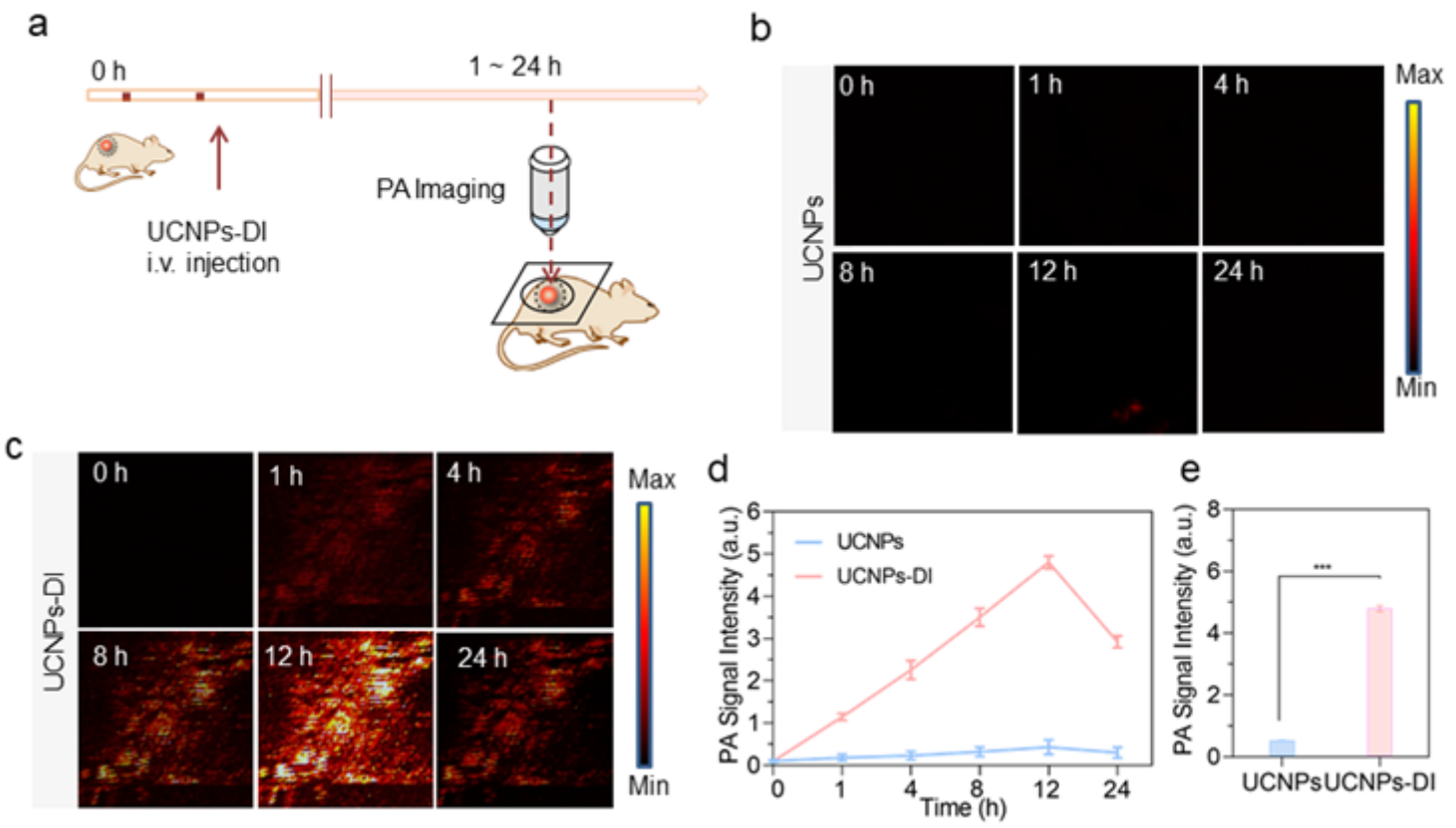

Figure 5

Photoacoustic imaging and distribution of UCNPs and UCNPs-DI. (a) Schematic illustration of photoacoustic imaging of UCNPs and UCNPs-DI. (b) and (c) Real-time photoacoustic images of the tumors after systematic administration of UCNPs and UCNPs-DI in nude mice. (d) quantitation of photoacoustic signal at the tumor site of UCNPs and UCNPs-DI. Mean values and error bars are defined as mean and SD, respectively (n = 3, mean ± SD). (e) Significance between the max PA signal two groups was calculated by a t test.

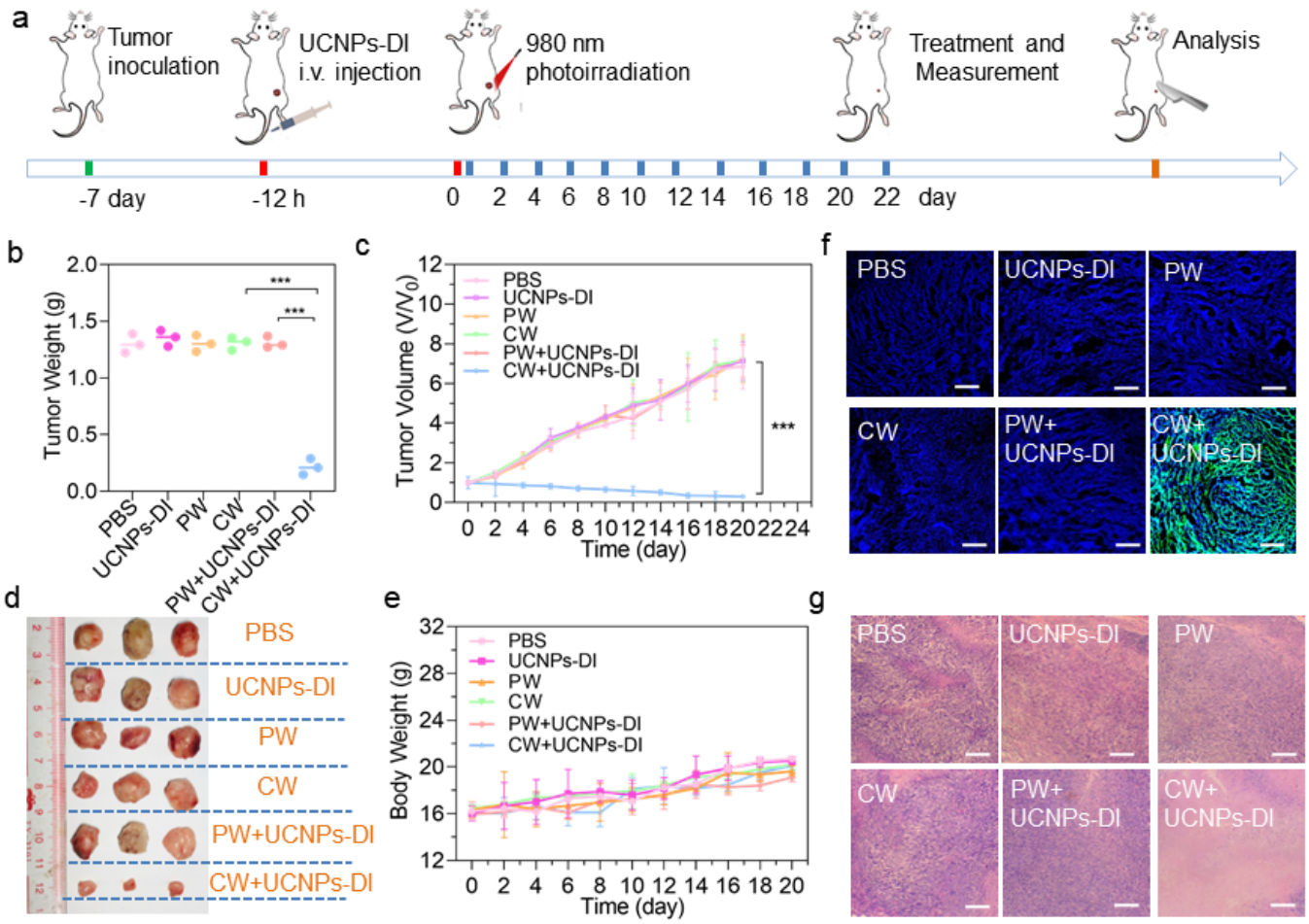

Figure 6

Orthogonally regulated tumor treatment. (a) Schematic illustration of the PDT treatment regimen. (b) Mean tumor weight at 21 days after treatment. (c) Tumor volume growth curve after with PBS, UCNPs-DI, PW, CW, PW+UCNPs-DI, and CW+UCNPs-DI. (d) Photograph of the tumor extracted from the mice and mean tumor weights at 21 days after treatment. (e) Changes in the mice body weights after different treatment. (f) SOSG immunofluorescence sections were treated in different groups. (g) H&E staining of tumor slices for treatments. Quantitative data are expressed as mean SD. p values were calculated by two-tailed Student s t-test (***p < 0.001, **p < 0.01, or *p < 0.05).

Supplementary Files

This is a list of supplementary files associated with this preprint. Click to download.

- TableofContents.docx
- Supportinginformation.docx